

# Numerical simulation of the landslide-generated tsunami in Kitimat Arm, British Columbia, Canada, 27 April 1975

A. Skvortsov<sup>1</sup> and B. Bornhold<sup>1</sup>

Received 13 March 2006; revised 21 November 2006; accepted 3 January 2007; published 31 May 2007.

[1] It remains challenging to predict and estimate potential damage from tsunamis using computer models. One of the approaches to validate models is to compare their results with site observations. We carried out numerical modeling for both the underwater landslide and the associated tsunami that occurred near Kitimat, British Columbia, Canada on 27 April 1975. A few observations of high water marks along the coastline indicated 8.2 m tsunami waves. Previous survey results of the seafloor showed that a landslide traveled about 5 km down the axis of the fjord from its source areas on the sidewall of the fjord, near the head of the inlet, and on the lower Kitimat River delta. We modeled the subaqueous slope failure as a Bingham visco-plastic fluid (debris flow) based on previous geotechnical investigations at the site, and numerically solved the landslide-generated tsunami wave and debris flow equations using a finite-volume Godunov-type scheme. This method resolves abrupt wave and landslide front interactions and remains oscillation-free. The computed motion of the debris flow is generally consistent with observations; simulations indicate that the failure propagated approximately 4.5 km down the fjord axis from its inception point. We have found that computed amplitudes for the tsunami wave crest at the coast of Kitimat Arm were between 6 and 11 m; these values are somewhat higher than previous simplistic solitary wave theory estimates of 6.3 m and observations of 8.2 m.

**Citation:** Skvortsov, A., and B. Bornhold (2007), Numerical simulation of the landslide-generated tsunami in Kitimat Arm, British Columbia, Canada, 27 April 1975, *J. Geophys. Res.*, 112, F02028, doi:10.1029/2006JF000499.

## 1. Introduction

[2] Tsunamis can be generated by submarine failures or by land masses sliding into the sea. Landslide-generated tsunamis can produce catastrophic waves often with significant coastal wave run-up. These tsunamis are more localized compared to earthquake related tsunamis, and can be amplified if the wave energy is trapped within the inlet or fjord. Most tsunami research in the past has focused on seismic tsunamis. Recently, after several destructive tsunamis caused by huge submarine landslides, more attention has been directed at improving our understanding of tsunamis produced by underwater slope failures [Tinti, 2002].

[3] The following are probably the largest documented landslide-generated tsunami events in the last 50 years: (1) In Lituya Bay, Alaska, on 10 July 1958 [Lander, 1996] a 517-m wave run-up generated by a landslide occurred after a southeastern Alaska earthquake. (2) In Vaiont Valley, Italy, on 9 October 1963 [Wiegel *et al.*, 1970] there was a massive rock slide into a reservoir, producing a wave that destroyed a town and killed 3000 people. (3) In Flores Island, Indonesia, on 12 December 1992 [Imamura and

Gica, 1996] submarine landslides during the Indonesian earthquake produced wave runup up of 26.2 m causing 1713 casualties. (4) In Papua, New Guinea, on 17 July 1998 [Tappin *et al.*, 1999] an earthquake triggered landslide generated tsunami waves up to 15 m which destroyed several villages and killed 2000 people.

[4] In many cases underwater landslides produce tsunamis that cause severe damage to port facilities and coastal structures. The earliest documented landslides in Kitimat Arm occurred in 1952–1968, 1971, and 1974; small amplitude tsunamis were observed during these events. On 17 October 1974, landslide generated tsunami waves reached 2.8 m at the coast. On 27 April 1975 a major landslide produced tsunami waves of much higher amplitude causing significant damage to coastal areas. The tsunami flooded all facilities in the upper delta of Kitimat Arm, damaging the Northland Navigation Wharf, destroying dolphins at the Eurocan Terminal, and carrying away shore installations at the First Nations settlement of Kitimaat 4 km across the inlet on the east shore. The maximum documented wave amplitude was 8.2 m [GolderAssociates, 1975; Murty, 1979].

[5] Simple solitary wave theory was used by [Murty, 1979] to estimate the wave heights associated with this event. The estimates were given without consideration of the area and essential slide characteristics, such as bathymetry, coastline configuration, and rheology. They also neglected the complicated interaction of waves evident in

<sup>1</sup>School of Earth and Ocean Sciences, University of Victoria, Victoria, British Columbia, Canada.

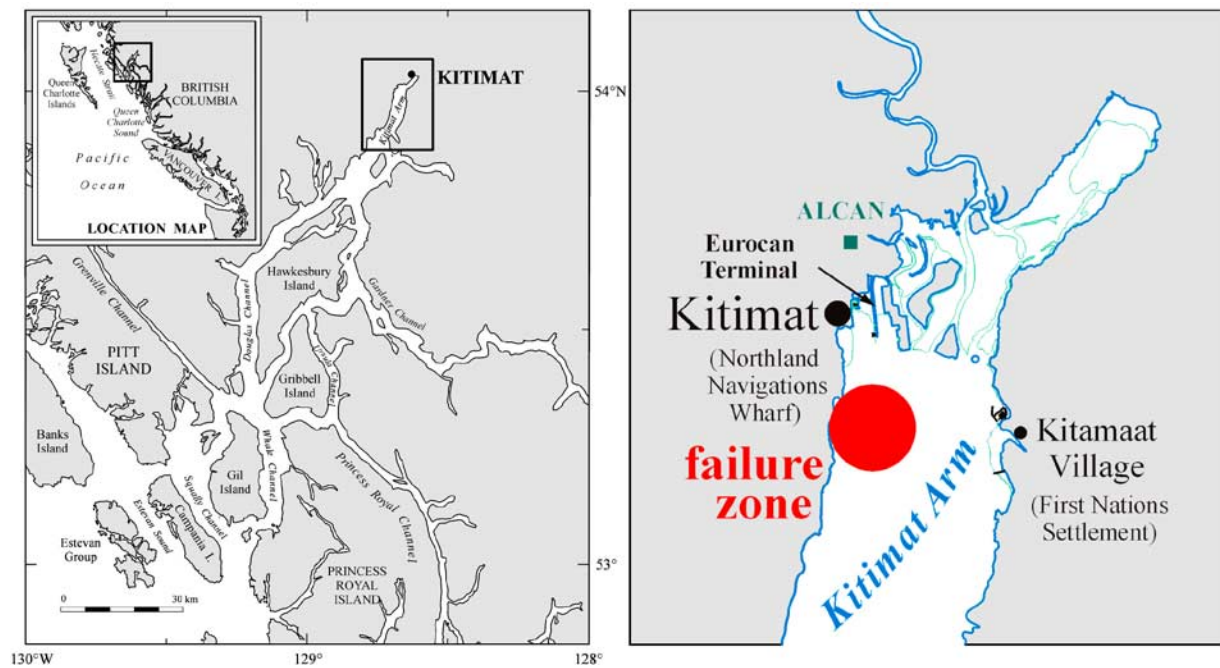


**Figure 1.** (left) Location map of British Columbia, Canada. Douglas channel system. (right) Kitimat Arm, located at the head of the Douglas Channel. The underwater landslide failure zone is indicated by a red circle.

2D/3D simulations. The main result was an analysis for the zone within 305 m of the slide origin and estimated a maximum 6.3 m height for the wave. In this work we attempt to improve on the previous modeling.

## 2. Kitimat Landslide, 27 April 1975

[6] Kitimat Arm is a part of Douglas Channel, a major fjord system on the northern coast of British Columbia, Canada (Figure 1). Douglas Channel is more than 70 km long and divided into several basins by moraines and bedrock sills. The floor of the basin has a general depth of 200–220 m in Kitimat Arm. The seafloor in the axis of the fjord and on the adjacent fjord walls is covered with gray marine muds [Bornhold, 1983].

[7] At 10:05 a.m. on 27 April 1975, a submarine slope failure occurred in Kitimat Arm. It happened approximately 53 min after an extreme low tide and was triggered by relatively minor construction operations on sediments that were in a state of critical equilibrium [Murty, 1979]. Two major landslides from the foreslope of the Kitimat River delta were involved: a large-scale failure of deltaic sediments and a landslide on the west wall of the fjord.

[8] The failed mass of delta and sidewall sediments (estimated volume  $27 \times 10^6 \text{ m}^3$ ) slid down into the fjord and apparently initiated the mobilization of a further  $28 \times 10^6 \text{ m}^3$  of fjord-bottom sediments, creating a massive, kilometer-wide debris flow of about  $55 \times 10^6 \text{ m}^3$ . The flow traveled over 5 km from the delta front over slopes of less than  $0.4^\circ$  to a water depth of 210 m. Individual blocks (outrunner blocks) of considerable size (up to  $35 \times 10^3 \text{ m}^3$ ) slid along the seafloor a farther 1 km beyond the main flow [Prior et al., 1984].

[9] The *GolderAssociates* [1975] report describes the failure: “The slump was reported to have started at the breakwater, and within about 2 min or so had worked its way around the shoreline along the road to the wharf. The log crib wharf structure was carried away by the slide. Slumping of the breakwater and shoreline was followed by propagation of the seawave, which fanned out from Moon Bay and struck Northland Navigation Wharf, Eurocan Terminal, and swept across the inlet to the Kitimaat Haisla village (Figure 1). Backward and forward oscillations of the water across the inlet were observed for over 1 hour after the initial event; the height of the wave was reported to have been 8.2 m at Kitimaat village on the basis of observations of water marks on pilings”. On the next day two further landslides occurred in the area of the wharf, but the events were of much smaller scale and no waves were reported [GolderAssociates, 1975].

## 3. Landslide-Tsunami Model

### 3.1. Model Description

[10] Modeling tsunamis generated by coastal and submarine landslides requires modeling the landslide motion. Existing landslide models used to produce tsunami waves can be classified into the following groups, depending on physical properties of the failure.

[11] 1. In solid body models [Heinrich, 1992], a rigid body slides as a whole along the slope with allowance made for friction between a bed surface and the slide.

[12] 2. Viscous or Newtonian models [Johnson, 1970; Jiang and LeBlond, 1992] are better suited to landslides involving fine-grained water-saturated deformable sediments or diluted muds.

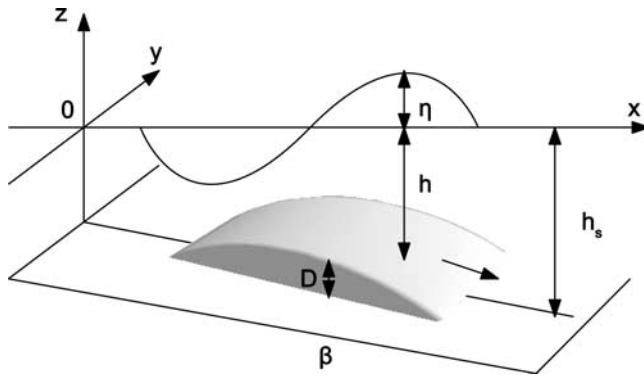


**Figure 2.** An isometric depiction of a landslide-generated tsunami model. The landslide is represented by a profile with a thickness  $D$  on an incline with slope  $\beta$ . Above the landslide is a water layer of depth  $h$ . The amplitude of the wave crest/trough is  $\eta$ . All the variables are functions of  $x$  and  $y$  coordinates.

[13] 3. Visco-plastic Bingham models [Liu and Mei, 1989; Jiang and LeBlond, 1993] unite the features of both of the above theories and incorporate a transition from solid body to viscous type models. Bingham visco-plasticity is most applicable to the dynamics of cohesive muds.

[14] While some models consider landslides as viscous, very few modeling studies of landslide-generated tsunamis consider the landslide as a Bingham fluid, a more general rheological model. Bingham visco-plastic models incorporate the transition from a solid body to viscous materials and hence have a potential advantage for simulating a broader range of landslide behavior. In the present study we apply a Bingham rheology model to the landslide and use 2D shallow water hydrodynamic equations to simulate tsunami waves in Kitimat Arm caused by the submarine failure on 27 April 1975.

[15] The main assumptions for the Bingham visco-plastic landslide and tsunami model are as follows.

[16] 1. The slide is an incompressible, Bingham fluid, and the seawater is an incompressible inviscid fluid.

[17] 2. The density difference between a flowslide and seawater is large, i.e.,  $(\rho_2 - \rho_1) \geq 0.2 \text{ g/cm}^3$ . The slide material can be diluted quickly owing to mixing at the water-mud interface at the brief initial stages of failure when mobilization of sediments takes place, but not during propagation. Thus density and Bingham rheology parameters are assumed to be constant.

[18] 3. The slide satisfies a long-wave approximation, implying that the width and length are much greater than its thickness. Velocity dominates in the  $x$  and  $y$  directions and pressure within the mud layer is assumed to be hydrostatic.

[19] 4. The surface waves satisfy the long-wave (hydrostatic) approximation, implying that the wavelength of the water waves is much greater than the water depth.

[20] A conceptual sketch of a Bingham slide and associated surface waves is presented in Figure 2. The standard Cartesian system of coordinates,  $x, y, z$  is used, with  $z$  directed vertically upward. The upper layer consists of seawater with density  $\rho_1$ , surface elevation  $\eta(x, y, t)$ , water depth from zero level  $h$ , total water column depth  $h_w = \eta + h$ , and horizontal  $(x, y)$  velocities  $u_w, v_w$ . The bottom layer (slide) velocities are denoted by  $u, v$ . The slide is bounded by an

upper surface  $z = -h(x, y, t)$  and a seabed surface  $z = -h_s(x, y)$ . The thickness of the slide is  $D = h_s(x, y) - h(x, y, t)$  and the constant density by  $\rho_2$ .

### 3.2. Equations for Bingham Landslide

[21] A Bingham material is a type of fluid which does not exhibit deformation until internal shear stress overcomes a threshold, called the yield stress, after which the deformation is driven by the excess of the stress beyond the yield stress. Many materials such as snow, volcanic lava, marine and river sediments behave approximately as Bingham plastic fluids [Mei and Liu, 1987]. Bingham rheology is determined by the equation

$$\begin{cases} \frac{\partial u}{\partial z} = 0 & \tau < \tau_0 \\ \frac{\partial u}{\partial z} = \frac{1}{\mu}(\tau - \tau_0) & \tau > \tau_0, \end{cases} \quad (1)$$

where  $\tau$  is the shear stress,  $\tau_0$  is the yield stress, and  $\mu$  is the coefficient of dynamic viscosity.

[22] Bingham rheology introduces two distinct zones in the debris flow: (1) a shear zone near the bottom and (2) an upper plug zone (Figure 3). According to Fine *et al.* [2003] conservation of mass and momentum for the Bingham visco-plastic slide can be expressed as

$$\begin{aligned} \frac{\partial u D}{\partial t} + \frac{\partial \alpha u^2 D}{\partial x} + \frac{\partial \alpha u v D}{\partial y} \\ = \frac{1}{\rho_2} \left( -D \frac{\partial \phi}{\partial x} - \frac{u}{U} \tau_0 (1 + d_1) - \frac{2\mu u}{D(1 - \frac{d_1}{3})} \right), \end{aligned} \quad (2)$$

$$\begin{aligned} \frac{\partial v D}{\partial t} + \frac{\partial \alpha u v D}{\partial x} + \frac{\partial \alpha v^2 D}{\partial y} \\ = \frac{1}{\rho_2} \left( -D \frac{\partial \phi}{\partial y} - \frac{v}{U} \tau_0 (1 + d_1) - \frac{2\mu v}{D(1 - \frac{d_1}{3})} \right), \end{aligned} \quad (3)$$

$$\frac{\partial D}{\partial t} + \frac{\partial u D}{\partial x} + \frac{\partial v D}{\partial y} = 0, \quad (4)$$

where  $\phi = \rho_2 g(D - h_s) + \rho_1 g h_w$  is the forcing potential with the acceleration due to gravity  $g$ . The water is assumed to have no effect on the landslide (i.e., no coupling); the forcing potential is then  $\phi = (\rho_2 - \rho_1)g(D - h_s)$

Nondimensional coefficient

$$\alpha = \frac{1 - \frac{7}{15}d_1}{(1 - \frac{1}{3}d_1)^2},$$

Shear layer relative to total thickness

$$d_1 = \sqrt{\kappa^2 + 2\kappa} - \kappa,$$

Visco-plastic ratio

$$\kappa = \frac{\mu|U|}{\tau_0 D(1 - \frac{d_1}{3})},$$

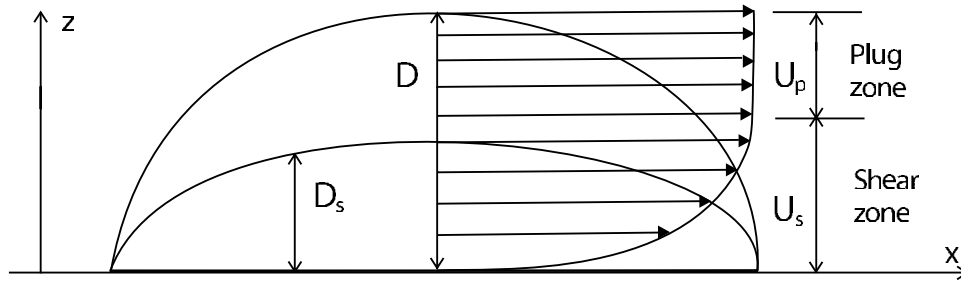


**Figure 3.** Bingham rheology flow cross section. The fluid profile consists of two layers: (1) the plug zone (upper layer) moves as an entity with a constant speed  $U_p$ , and (2) the shear zone (bottom layer) has a parabolic velocity profile  $U_s(z)$ .

Full velocity

$$U = \sqrt{u^2 + v^2}.$$

[23] Simple analysis shows that for  $d_1 \rightarrow 0$  we get  $\alpha \rightarrow 1$ . If this is the case, the plug layer in the Bingham flow becomes dominant and the fluid solidifies. If  $d_1 \rightarrow 1$ , we get  $\alpha \rightarrow 1.2$  and a shear layer dominates as the fluid becomes Newtonian. In the extreme case if  $d_1 = 1$  the equations (2)–(4) will transform to the equations for a viscous slide.

[24] The slide initiation requirement is that the driving force must exceed the yield stress  $\tau_0$ :

$$D|\nabla\phi| > \tau_0. \quad (5)$$

[25] The initiation requirement (5) also means that if the driving force falls below the yield stress a Bingham fluid in motion will eventually stop on the slope. For a uniform mud layer on an underwater slope with no elevation at the water surface, the expression (5) can be transformed to obtain the critical thickness at which deposits can remain stationary on a slope with an inclination of  $\beta$ .

$$D_c = \frac{\tau_y}{(\rho_2 - \rho_1)g \sin \beta}. \quad (6)$$

Thus a uniform mud layer remains stationary on a slope if its thickness  $D$  is smaller than  $D_c$ . In contrast to Newtonian fluids it can achieve a state of equilibrium.

### 3.3. Equations for Surface Waves

[26] The upper layer (water) is governed by the nonlinear shallow water equations:

$$\frac{\partial h_w u_w}{\partial t} + \frac{\partial}{\partial x} \left( h_w u_w^2 + \frac{1}{2} g h_w^2 \right) + \frac{\partial}{\partial y} (h_w u_w v_w) = g h_w \frac{\partial h}{\partial x}, \quad (7)$$

$$\frac{\partial h_w v_w}{\partial t} + \frac{\partial}{\partial y} \left( h_w v_w^2 + \frac{1}{2} g h_w^2 \right) + \frac{\partial}{\partial x} (h_w u_w v_w) = g h_w \frac{\partial h}{\partial y}, \quad (8)$$

$$\frac{\partial h_w}{\partial t} + \frac{\partial (h_w u_w)}{\partial x} + \frac{\partial (h_w v_w)}{\partial y} = 0. \quad (9)$$

[27] Equation (9) is the continuity equation and (7) and (8) are the momentum equations along the  $x$  and  $y$  Cartesian

coordinates. The slide generates water waves through the continuity equation (9) only.

### 3.4. Numerical Approach

[28] Nonlinearity combined with the hyperbolic character of the shallow water equations (SWE) (2)–(4) and (7)–(9) makes finding their solution difficult. The numerical solution of the SWE for gravity-driven flows or wave propagation over real domains poses three specific difficulties: (1) Simulation of flow fronts or abrupt water waves that can be represented numerically as propagating discontinuities. (2) Abrupt changes in bathymetry. As long as the bottom surface remains sufficiently smooth, most numerical techniques provide an accurate solution of the flow, but if the bottom surface is very rough most methods fail. (3) Front propagation over a dry bed; i.e., where landslide thickness is zero. To address these problems we utilize Godunov's finite volume scheme, suitable for handling complex topography. The method considers local initial value problems which involve discontinuous neighboring states in the computational domain. Discontinuous initial value problems are known as Riemann problems (Figure 4) and mathematically can be expressed as

$$Q(x, t) = \begin{cases} Q_L(x, t) & x < 0 \\ Q_R(x, t) & x > 0 \end{cases}, \quad (10)$$

where  $Q$  is a given function of  $x$  and  $t$  in the numerical domain, such as velocity, height or pressure. The Riemann

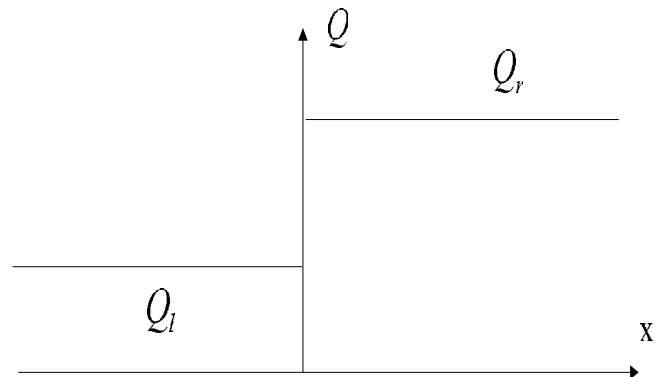


**Figure 4.** Riemann problem: initial value problem at the cell interfaces in the Godunov schema.  $Q_L$  and  $Q_R$  denote the left and right state of variables at the discontinuity.



problem solution is the evolution of fluid initially composed of two states with different and constant values of  $Q$ .

[29] The Godunov method [Godunov *et al.*, 1979] solves Riemann problems arising at each cell interface using a cell-wise constant finite-volume scheme. The Riemann problem solution for hyperbolic equations is a finite set of waves, which are shocks or rarefaction waves propagating from the interfaces between the grid cells.

[30] To prepare for the numerical solution, the set of equations (7)–(9) can be rewritten in vector form (11), where the overbar denotes a three-component vector. The procedure is analogous for the landslide equations (2)–(4).

$$\begin{aligned} \frac{\partial \bar{Q}}{\partial t} + \frac{\partial \bar{F}_x}{\partial x} + \frac{\partial \bar{F}_y}{\partial y} &= \bar{S}, \\ \bar{Q} &= \begin{pmatrix} h_w \\ uh_w \\ v h_w \end{pmatrix} \quad \bar{S} = \begin{pmatrix} 0 \\ h_w g \frac{\partial h}{\partial x} \\ h_w g \frac{\partial h}{\partial y} \end{pmatrix}, \\ \bar{F}_x &= \begin{pmatrix} u h_w \\ u^2 h_w + g \frac{h_w^2}{2} \\ u v h_w \end{pmatrix} \quad \bar{F}_y = \begin{pmatrix} v h_w \\ v u h_w \\ v^2 h_w + g \frac{h_w^2}{2} \end{pmatrix}. \end{aligned} \quad (11)$$

In order to solve a multidimensional problem using Godunov's scheme it is convenient to apply the fractional step method of Yanenko [1971]. The set of equations (11) is split into two 1D systems with a separation of derivatives for  $x$  and  $y$  Cartesian coordinates respectively.

$$\frac{\partial \bar{Q}}{\partial t} + \frac{\partial \bar{F}_x}{\partial x} = \bar{S}_x \quad \bar{S}_x = \begin{pmatrix} 0 \\ h_w g \frac{\partial h}{\partial x} \\ 0 \end{pmatrix} \quad (12)$$

$$\frac{\partial \bar{Q}}{\partial t} + \frac{\partial \bar{F}_y}{\partial y} = \bar{S}_y \quad \bar{S}_y = \begin{pmatrix} 0 \\ 0 \\ h_w g \frac{\partial h}{\partial y} \end{pmatrix}. \quad (13)$$

[31] The Godunov procedure is applied to each 1D system above (equations (12) and (13)). As a finite volume method, Godunov's scheme of first order for conservational 1D SWE can be now formulated as

$$\bar{Q}_i^{n+1} - \bar{Q}_i^n = -\frac{\Delta t}{\Delta x} (\bar{F}_{i+1/2} - \bar{F}_{i-1/2}) + \Delta t \bar{S}. \quad (14)$$

[32] The numerical flux function  $\bar{F} = (\bar{F}_x, \bar{F}_y)$  is the flux computed from the exact or approximate solution  $\bar{Q}_i^*$  of the Riemann problem, taken at the location of the cell interfaces

$$\bar{F}_{i+1/2} = \bar{F}(\bar{Q}_i^*(x_{i+1/2})) \quad \bar{F}_{i-1/2} = \bar{F}(\bar{Q}_i^*(x_{i-1/2})), \quad (15)$$

where

$$\bar{Q}_i^*(x_{i+1/2}) = \bar{Q}_i^*(\bar{Q}_i, \bar{Q}_{i+1}) \quad \bar{Q}_i^*(x_{i-1/2}) = \bar{Q}_i^*(\bar{Q}_{i-1}, \bar{Q}_i) \quad (16)$$

is the exact or approximate solution of the Riemann problem (10) [Toro, 2001]. Many efficient Riemann solvers are available such as Roe's [Roe and Pike, 1984], HLL [Harten *et al.*, 1983], HLLC [Toro *et al.*, 1994], Osher-Solomon [Osher and Solomon, 1982], Vanleer [van Leer, 1977, 1985] and others. In this work the HLLC solver has been utilized for the solution of landslide and wave equations.

[33] The systems of equations (2)–(4) and (7)–(9) are subject to the boundary conditions. It is assumed that there is no slide transport through the coastal boundary and that the slide does not reach the open boundary. For the system of tsunami wave equations (7)–(9) we prescribe transmissive conditions at the open boundary, setting

$$\begin{cases} h_0^n = h_1^n, & u_0^n = u_1^n, \\ h_{m+1}^n = h_m^n, & u_{m+1}^n = u_m^n. \end{cases} \quad (17)$$

At the coast solid reflective boundaries are imposed as

$$\begin{cases} h_0^n = h_1^n, & u_0^n = -u_1^n, \\ h_{m+1}^n = h_m^n, & u_{m+1}^n = -u_m^n. \end{cases} \quad (18)$$

[34] The theoretical model and the finite volume Godunov scheme are formulated in a conservational form. Numerical tests revealed that the scheme is stable and does not give rise to oscillations in the presence of discontinuities. In practice, because the landslide equations have complex source terms, some numerical diffusion occurs. While this may lead to underestimation of maximum tsunamis heights and smoother landslide profiles, the volume and the momentum are both conserved. A detailed description along with the comparison between numerical and analytical solutions are given by Skvortsov [2005]. Mathematical description and application of the Godunov scheme and comparisons of various robust solvers for the SWE are thoroughly discussed by Toro [2001].

### 3.5. Model Parameters

[35] The process of water wave generation is controlled by the characteristics of the landslide such as volume, location, and rheology. Several physical quantities affect run-out distance, thickness, and velocity of the slide. These include viscosity and yield stress of the slide, and densities of water and the slide sediments. Some researchers have provided sensitivity and experimental analysis of these factors [Locat and Lee, 2002; Rabinovich *et al.*, 2003]. For example, a change in density by 20% results in an increase in simulated wave amplitudes of 20%; however for density variations  $\leq 0.1 \text{ g cm}^{-3}$ , changes in tsunami wave heights are negligible [Rabinovich *et al.*, 2003]. From laboratory experiments it has been shown that the yield strength contributes about 1000 times more than the viscosity to the resistance to flow of the fluid [Locat and Lee, 2002].

[36] In order to obtain Bingham slide parameters for the present modeling, sediment samples obtained near Kitimat were used (Core 4 from Prior *et al.* [1984]). The Core 4 samples were taken several kilometers downfjord within the

main deposits. They show a mixture of silt (56%) and clay (43%) with only a very small amount of sand (<1%); water contents are high and generally decline with depth. Laboratory values of water and slide densities are  $\rho_w = 1 \text{ g/cm}^3$  and  $\rho_s = 1.65 \text{ g/cm}^3$ , respectively [Prior *et al.*, 1984; Johns *et al.*, 1985].

[37] Values of yield stress and viscosity for the Bingham material are not straightforward to obtain. Geotechnical measurements of sediment static resistance for Kitimat samples indicate a shear strength of the order of 25–40 kPa, at least 4 times larger than the yield stress required for failure. Much lower yield stresses occurred during the event [Johns *et al.*, 1985].

[38] The substantial decrease in the yield stress can be associated with the extensive remolding and mobilization of the landslide during the first stages of failure. There is also a process of intensive dilution at the interface between the water and the slide; this together with the above mechanism causes water entrainment into deeper sections of the landslide. All these factors can bring about a significant reduction in yield stress to 0.5–3 kPa [DeBlasio *et al.*, 2003]. It has been assumed that this reduction in yield stress occurs instantaneously after the failure inception and the yield stress remains nearly constant during the landslide run.

[39] It has been proposed by Locat and Lee [2002] and Locat [2001] that the yield stress and dynamic viscosity could be related to the liquidity index  $I_L$ . Their experimental results indicated that these can be estimated from the following empirical formulas:

$$\tau_0 = \left( \frac{5.81}{I_L} \right)^{4.55}, \quad (19)$$

$$\mu = \left( \frac{9.27}{I_L} \right)^{3.3}, \quad (20)$$

$$I_L = \left( \frac{w_n - w_p}{w_L - w_p} \right), \quad (21)$$

where  $w_n$  is the natural water content, and  $w_L$  and  $w_p$  are the liquid and plastic limits, respectively. For the computations, lower values of water content (those in deeper parts of the slide) [Prior *et al.*, 1984] are chosen with plastic and liquid limits of the material in Core 4. On the basis of these considerations the following settings for the computations were derived from formulas (19)–(21): kinematic viscosity  $\nu = 0.01 \text{ m}^2/\text{s}$ , yield stress  $\tau_0 = 2.5 \text{ kPa}$ .

[40] The digitized numerical domain for the Kitimat region has grid dimensions of  $300 \times 187$  with spatial grid cell size  $\Delta x = \Delta y = 20 \text{ m}$ . The time steps are  $\Delta t = 0.025 \text{ s}$  and  $\Delta t = 0.2 \text{ s}$  for a landslide and tsunami waves respectively.

## 4. Results of Numerical Modeling

[41] Numerical simulations were intended to answer the following questions. (1) What were the wave heights and timings of the arrival of the landslide-generated tsunami waves around Kitimat Arm? (2) What were the maximum speed, propagation distance, and thickness of the debris flow?

### 4.1. Landslide Modeling

[42] Figures 5 and 6 are snapshots of the flow debris failure. The landslide exhibits a complex motion, especially during the initial phase of collapse (i.e., first 30 s). During this period the slide accelerates because of the steep bottom slopes (up to  $14^\circ$ ) and local slopes in the slide body itself. It exhibits complex mobilization and reorganization transforming itself into a debris flow. Half of the volume comes from the side wall in a direction perpendicular to the axis of the inlet. Two fronts collide and merge to produce a massive flow moving southward along the fjord.

[43] The maximum speed (22.5 m/s) is reached after 19 s. After this moment the slide driving force decreases, because the slide reaches an area of lower seafloor slope. The internal friction becomes dominant leading to the gradual reduction in slide velocity until it stops, approximately 4 min 30 s after the inception of failure. Most of the slide sediments stop closer to the delta as they do not attain enough acceleration to run over the gentle slopes ( $\lesssim 0.5^\circ$ ) of the seafloor. The thickest part of the slide (18 m) found after the landslide stopped is located in the delta front area. The slide front thickness is 4.3 m with a run-out distance of about 4.5 km, in good agreement with sea floor observations. (See Animation 1<sup>1</sup>.)

### 4.2. Tsunami Modeling

[44] Coastal boundaries and associated model boundary conditions are an important part of tsunami modeling. The east and west sides of the inlet are generally steep and thus reflective boundary conditions are appropriate. At the outer (southern) part of the domain a radiative boundary condition has been applied. Minette Bay at the head of Kitimat Arm is an extremely shallow area (most of the time there is no water in it), and the landslide failure occurred during a very low tide. The seafloor in the bay is very rough which is apparently why the wave could not have penetrated far into or propagated through Minette Bay [Murty, 1979]. The upper delta front boundary has thus been modeled as a wall.

[45] Snapshots of the wave evolution generated by the landslide are presented in Figure 7. During the first phase of the failure ( $\sim 20 \text{ s}$  after inception), a positive wave (crest) grows in front of the submarine slide; a negative wave (trough) significantly reduces the water level in the generation region. During the second phase (after  $\sim 20 \text{ s}$ ) the wave crest leaves the area above the slide and propagates toward the east coast. During the third phase (after  $\sim 70 \text{ s}$ ) waves on both sides of the fjord are reflected from the boundaries. Following these wave reflections from the coastline, tsunami waves form a complicated pattern of motions in the inlet.

[46] The coastal regions of greatest interest in terms of wave run-up and destruction are shown in Figure 1 and labeled as follows in Figure 7: the Eurocan Terminal (T) positioned at the delta, the Northlands Navigation Wharf (W) located at the source of the landslide, and the Kitimaat Haisla First Nations settlement (S) located on the opposite side of the inlet.

[47] Simulated wave records (Figure 8) provide wave characteristics for these sites. During the first 40 s of the

<sup>1</sup>Animations are available in the HTML.

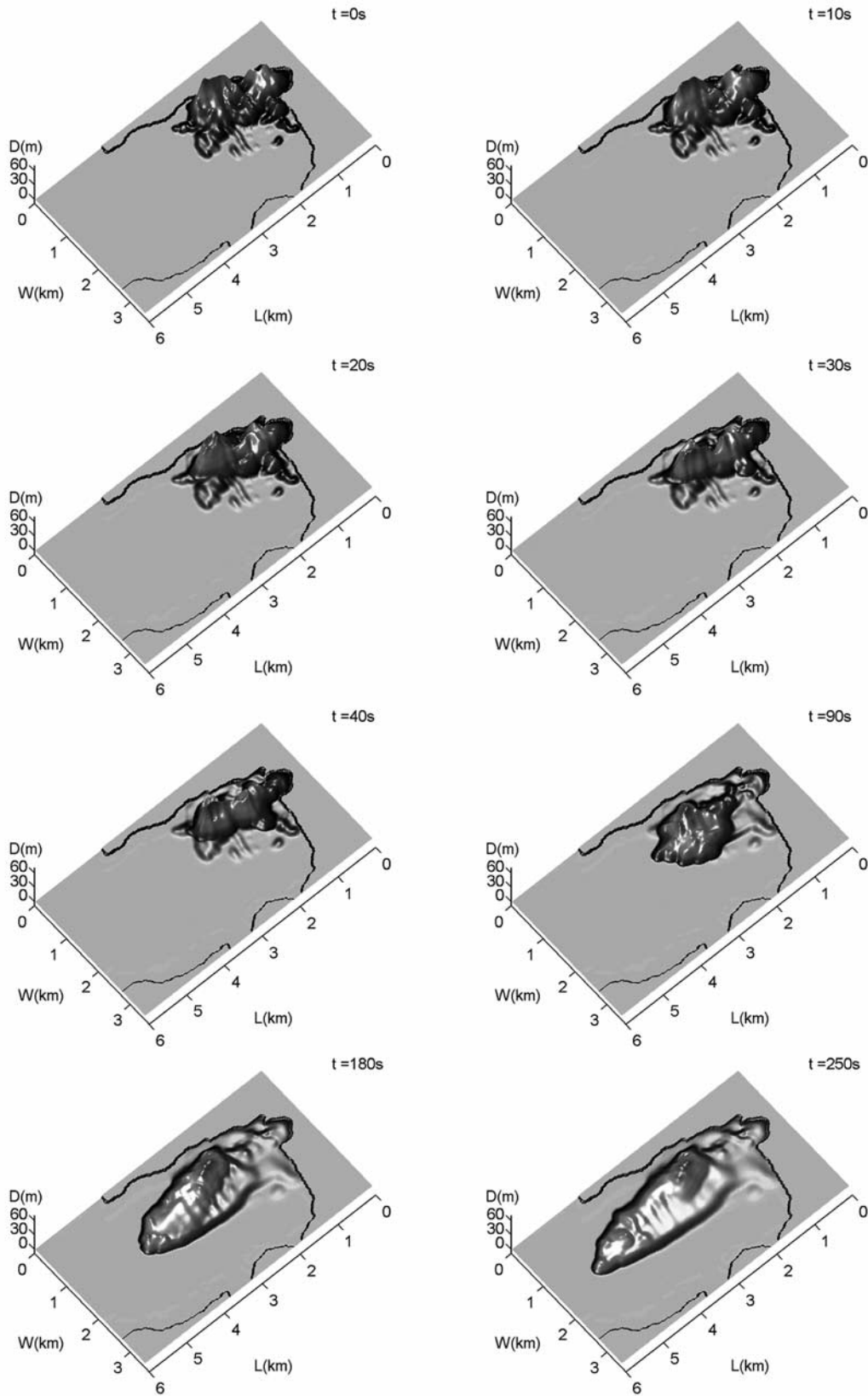


**Figure 5.** Snapshots of the modeled landslide profile showing its deformation during propagation down the fjord during the 27 April 1975 event. The vertical axis is the thickness of the landslide. Note two fronts from the side wall and the delta merging into a massive landslide during the first minute. Landslide sediments eventually stop on the bed surface when shear velocity falls below a yield stress for the Bingham fluid.

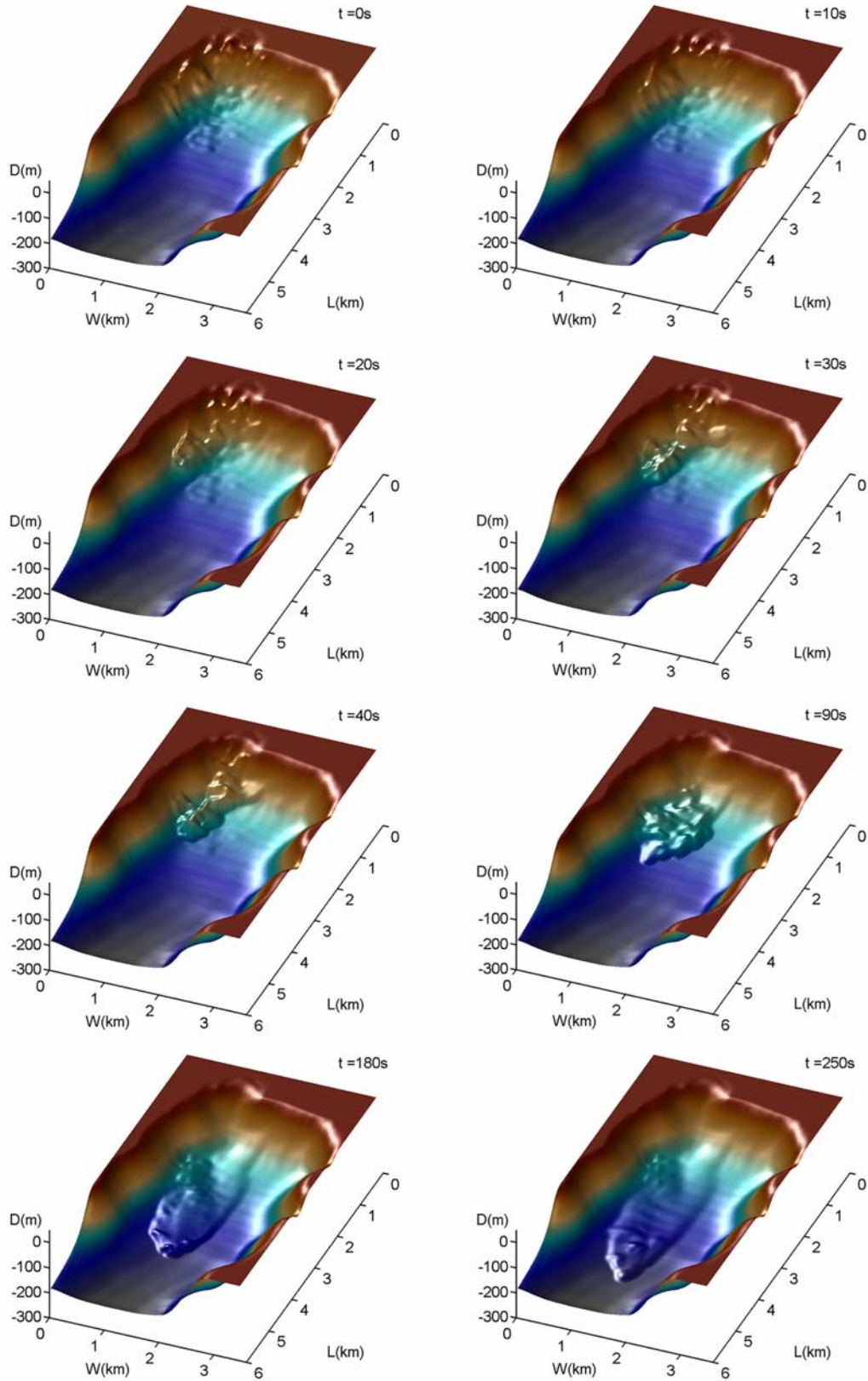


**Figure 6.** Snapshots of the modeled landslide propagating down the fjord axis over the underlying bed surface. The vertical axis is the depth of the fjord. The maximum landslide run out distance is 4.5 km at depth of 250 m in 285 s.



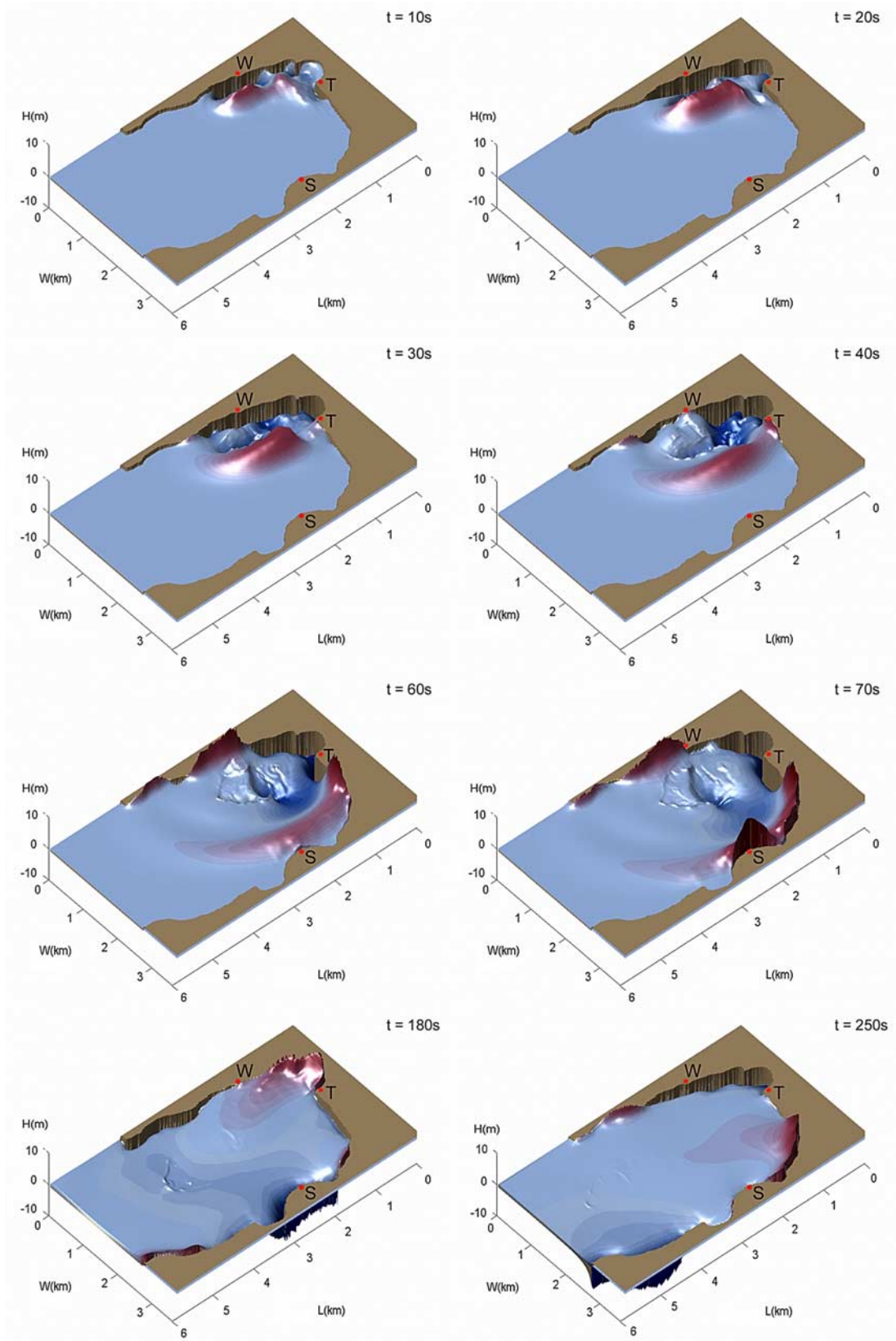


**Figure 7.** Snapshots of the modeled tsunami wave field generated by the modeled underwater landslide (Figures 5 and 6). The water level at locations marked by red dots is plotted in Figure 8. The vertical axis represents variations in sea level relative to the undisturbed state. The highest wave struck the eastern side of the fjord, at the location of the Kitamaat Village, 72 s after landslide inception. Note the wave trough at Eurocan Terminal after 40 s and the crest after 180 s.

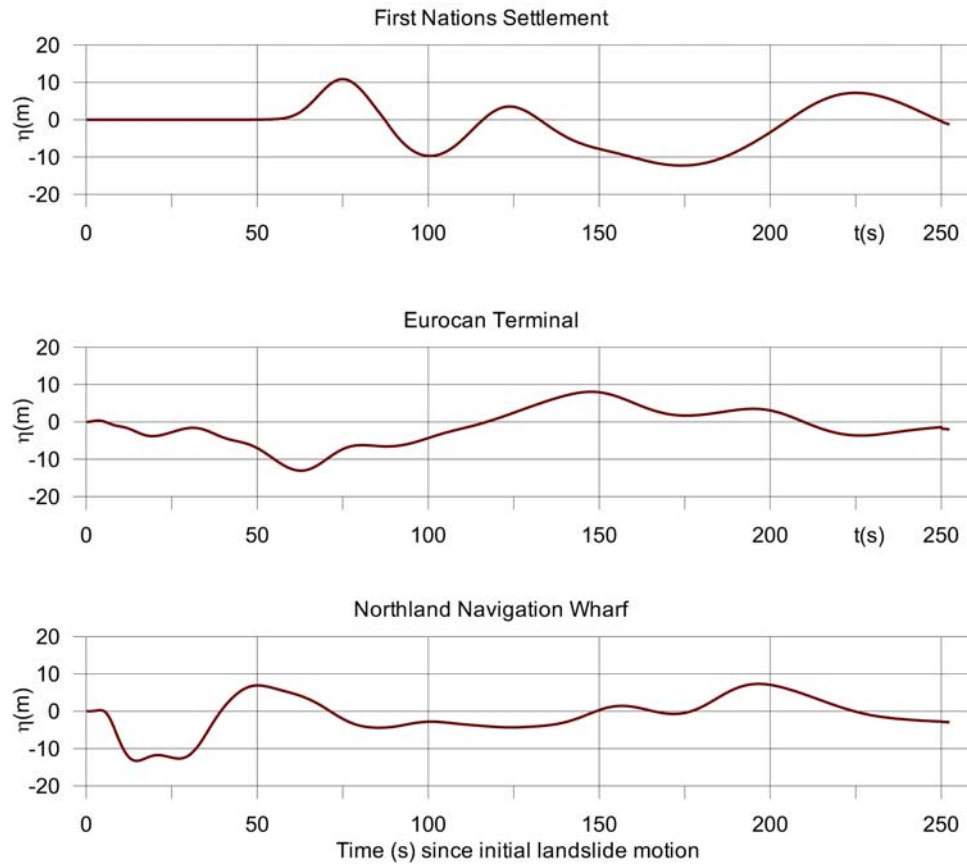


**Figure 8.** Modeled Kitimat sea levels during the 1975 tsunami for three different locations: Kitamaat Village First Nations Settlement on the east side of the fjord; Eurocan Terminal on the delta front; and, Northland Navigation Wharf on the west side near the landslide inception point. In Figure 7 these places are marked as S, T, and W, respectively. Note the maximum wave crest (10.9 m) near the Kitamaat Village, which is coincident in time with a trough at the Eurocan Terminal, and the prolonged flooding of the Eurocan Terminal and Northland Navigation Wharf several minutes later.

slide failure, water recession in the area of the Eurocan Terminal and Northland Navigation Wharf is observed. The minimum trough amplitude is  $-13.3$  m at 15 s for the Northland Navigation Wharf and is quickly followed by a short 6.9 m crest wave after about 50 s. The highest wave hit the opposite side of the inlet where a crest arrived at the Haisla settlement in 72 s reaching a maximum height of 10.9 m at the coast. Although the Eurocan Terminal is located very close to the slide area, the destructive impact occurred there 2 min after the inception of the slide with the wave crest reaching 7 m. This destructive wave had the longest period and should have substantially flooded the area; water retreat occurred only after 4–5 min. A secondary crest hit the Navigation Wharf in 3 min 20 s and had an amplitude similar to that of the first wave. This was the main tsunami crest, which had reflected from the opposite side of the fjord (east coast). (See Animation 2.)

[48] In order to analyze the effectiveness and duration of the tsunami generation by the underwater failure we can introduce a characteristic based on the sea surface potential energy, associated with the vertical displacement of the water surface.

$$W = \iint_{\Omega} g\eta \frac{\partial D}{\partial t} ds. \quad (22)$$

[49] According to *Fine et al.* [2002] the equation (22) describes the transfer rate of mechanical energy to the sea surface integrated over the entire domain  $\Omega$ , where  $\eta$  is a water surface vertical displacement,  $g$  is acceleration due to gravity,  $D$  is the thickness of the landslide at the location  $s$ . Changes in the energy transfer rate in time are illustrated in Figure 9 and show the initial phase of landslide failure is the most important in terms of tsunami generation. Between 10–30 s, the highest energy transfer rate is reached with a

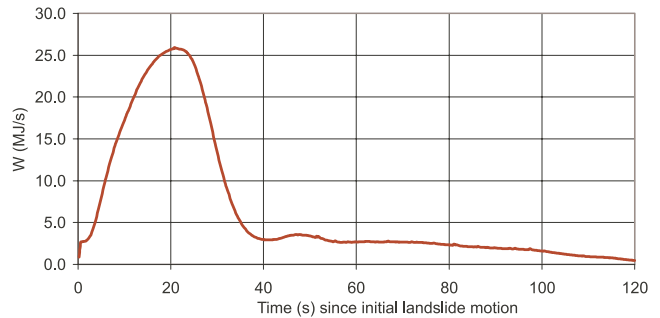


**Figure 9.** Changes in energy transfer rate, integrated over the entire domain, from the landslide to the water surface during failure. The most intensive wave generation is observed after about 20 s.

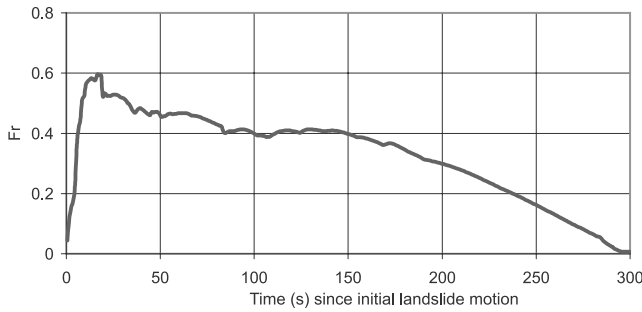


**Figure 10.** Froude number changes calculated for the landslide front velocity during the propagation of the debris flow. The Froude number attains values of less than 1 indicating that the underwater landslide velocities are subcritical.

peak of 26.5 MW; about 70% of the total energy transfer from the slide to surface waves occurs during this short period of time. This result correlates well with another characteristic: the maximum slide velocity is reached 19 s after the initiation of failure: the time close to the moment of maximum wave height generation. As the slide peak velocity is attained and starts declining after 20–30 s, the energy transfer is significantly reduced. The total energy transferred to waves is 550 MJ for this model simulation.

[50] An important characteristic of the landslide-wave system is the Froude number. The Froude number is usually computed for rigid-body slides, which move as an entity. In contrast, different parts of a visco-plastic slide move with different speeds. In this case the Froude number can be defined as the ratio of the slide front velocity to the local long-wave speed [Fine *et al.*, 2002].

$$F_r = \frac{u_f}{\sqrt{gh}}. \quad (23)$$

[51] Variables in equation (23) are  $u_f$ , the slide front velocity, and  $h$ , the water column thickness. The computed Froude number (Figure 10) rises significantly during the initial phase of the failure owing to the increasing velocity and shallower water depth. The maximum Froude number is 0.59 between 18 and 20 s and is less than the value ( $F_r = 1$ ) needed to achieve a resonant state or supercritical motion. The relatively flat area of the plot between 70 and 180 s indicates stable values of the Froude number around 0.4. At this time the slide moves with an average speed of 17–18 m/s over a gently sloping seafloor (slope  $\sim 0.5^\circ$ ). Decreasing Froude number values occur when the slide slows down and stops in 285 s.

## 5. Comparison With Other Studies and Targets for Future Work

[52] The most important feature of the model is its ability to capture all of the topographic details of the slide and bathymetry. Providing that the sediment rheology model is adequate and parameters are chosen correctly, the model should provide a competent landslide simulation and the basis for wave modeling. In fact, there are still certain conditions or processes which may have occurred during the failure, but which are difficult to constrain. The follow-

ing are some of these conditions and are targets for future investigation.

[53] Previous investigations [Prior *et al.*, 1984] have shown that some of the sediment within the debris flow deposit was apparently incorporated from the fjord basin floor. This would clearly introduce an additional volume and would influence the dynamics of the slide. This may not affect surface waves significantly, however, because the incorporation would take place in deep water and would not significantly increase the slide elevation over the seafloor.

[54] Earlier geological and geophysical studies showed that hydroplaning or block gliding occurred beyond the toe of the main debris flow deposit. A lubricating effect can occur at certain velocities and is achieved by water intrusion beneath the debris flow. If hydroplaning is established the slide run out distance and velocity become independent of rheology because of low friction between the slide and the sea bed. Hydroplaning is likely to occur on low slopes [Mohrig *et al.*, 1999]. In Kitimat Arm there are known outrunner blocks, i.e., sediments that traveled farther than the main volume of the slide and explained by hydroplaning.

[55] There were known to have been minor retrogressive failures during the 1975 event in Kitimat Arm. These are later consecutive slides triggered by the main slide. The current modeling accounts only for the instantaneous and simultaneous failure of all sediments; that is, the two main parts of the slide (sidewall and delta front) collapse simultaneously.

[56] Inhomogeneity of the moving material, i.e., varying rheology and density. The entrainment of water promoted by the landslide motion causes dilution of sediments thus resulting in rheology changes. Parameters such as yield stress and viscosity used in the Bingham rheology can be locally highly variable. Moreover, the complicated structure of landslide sediments can lead to significant rheological deviations from the imposed model.

[57] Campbell and Skermer [1975] mentioned that the duration of the slide could have been about 2 min; Murty [1979] estimated it as 0.5 min. Current modeling suggest that the slide traveled for around 4.5 min, which also agrees well with run out distances and average speeds.

[58] The numerical modeling results show extreme wave crests of 6 to 11 m generated in Kitimat Arm and provide estimates of wave amplitudes in the region. Times for wave propagation across the fjord (2 km) are about 1 min 30 s. The height estimate by Murty [1979], was 6.3 m, measured from trough to crest. The crest itself by Murty's calculations was 4.3 m [Murty, 1979], significantly lower than both actual observations and the results of this modeling study.

[59] Unfortunately it is not possible to obtain measured run-ups for the area and provide accurate comparisons, as there was no tide-gauge at Kitimat. Only a few observations based on high water marks at the coast are available. In the report by GolderAssociates [1975] it is stated that waves of 8.2 m were generated at the coast near the Haisla Settlement. The results of the present research closely agree with these observations.

## 6. Conclusions

[60] Our modeling of the 27 April 1975 subaqueous slope failure and tsunami in Kitimat Arm yielded results that were



more consistent with both seafloor surveys and tsunami observations than previous analyses. We modeled the debris flow as a Bingham visco-plastic material and solved the landslide-generated tsunami wave and debris flow equations numerically using a finite-volume Godunov-type scheme. The resulting simulations showed a debris flow run-out distance down the axis of the fjord, exclusive of hydroplaning, of 4.5 km from the source, very close to that observed in seafloor surveys. The simulated tsunami wave amplitudes around the head of Kitimat Arm were between 6 and 11 m, in agreement with observations at the time of the event of 8.2 m and somewhat higher than previous simplistic solitary wave theory estimates of 6.3 m.

[61] Many subaqueous failures evolve rapidly into debris flows. In such cases, Bingham landslide rheology is thus an appropriate and flexible model. Owing to its intrinsic ability to model sediments in static equilibrium, it can be used in simulations which require incorporation of sediments from the seabed during failure.

[62] We conclude that in such models of subaqueous landslide behavior abrupt topographic features do not cause instabilities if a robust Godunov scheme and solver are used. Even greater accuracy could be achieved if higher-order Godunov methods were used.

[63] There remain other important aspects of such landslide-generated tsunami events that should be addressed to improve our modeling capabilities and especially our ability to predict potential impacts in coastal areas. Of these wave run-up estimates at the coast and modeling of subaerial landslides entering coastal bays and inlets are the most important.

[64] **Acknowledgments.** We would like to thank Isaac Fine, Rick Thomson, and Chris Garrett for invaluable suggestions and advice during the course of this research. The manuscript was greatly improved by the very helpful suggestions made by an anonymous reviewer. This work was supported by a grant from the Natural Sciences and Engineering Research Council of Canada as part of the COSTA-Canada Program.

## References

- Bornhold, B. (1983), Sedimentation in Douglas Channel and Kitimat Arm, *Can. Tech. Rep. Hydrogr. Ocean Sci.*, 18, 88–114.
- Campbell, D., and N. Skermer (1975), Investigation of sea wave at Kitimat, BC, report, 9 pp., BC Water Resour. Serv., Victoria, B. C., Canada.
- DeBlasio, F., D. Issler, A. Elverhoi, C. Harbitz, T. Ilstad, P. Bryn, R. Lien, and F. Lovholt (2003), Dynamics, velocity and run-out of the giant Storegga slide, in *Submarine Mass Movements and Their Consequences*, edited by J. Locat and J. Mienert, pp. 223–230, Elsevier, New York.
- Fine, I., A. Rabinovich, R. Thomson, and E. Kulikov (2002), Numerical modeling of tsunami generation by submarine and subaerial landslides, *Earth Environ. Sci.*, 21, 69–88.
- Fine, I., A. Rabinovich, R. Thomson, E. Kulikov, and B. Bornhold (2003), Numerical simulation of landslide-generated tsunamis: Three different models, *Geophys. Res. Abstr.*, 5, 01791.
- Godunov, S., A. Zhabrodine, M. Ivanov, A. Kraiko, and G. Prokopov (1979), *Solution of Numerical Problems in Gas Dynamics*, MIR, Moscow.
- GolderAssociates (1975), Report to B.C. Water Resources Service on investigation of seawave at Kitimat, B.C., *Tech. Rep. 9/87*, B. C. Water Resour. Serv., Vancouver, B. C., Canada.
- Harten, A., P. Lax, and B. van Leer (1983), On upstream differencing and Godunov-type schemes for hyperbolic conservation laws, *SIAM Rev.*, 25, 35–61.
- Heinrich, P. (1992), Nonlinear water waves generated by submarine and aerial landslides, *J. Waterw. Port Coastal Ocean Eng.*, 118, 249–266.
- Imamura, F., and E. Gica (1996), Numerical model for tsunami generation due to subaqueous landslides along a coast, *Sci. Tsunami Haz.*, 14, 13–28.
- Jiang, L., and P. LeBlond (1992), The coupling of a submarine slide and the surface waves which it generates, *J. Geophys. Res.*, 97, 12,731–12,744.
- Jiang, L., and P. LeBlond (1993), Numerical modeling of underwater Bingham plastic mudslide and the waves which it generates, *J. Geophys. Res.*, 98, 10,303–10,317.
- Johns, M., D. Prior, B. Bornhold, J. Coleman, and W. Bryant (1985), Geotechnical aspects of a submarine slope failure, Kitimat Fjord, British Columbia, *Mar. Geotechnol.*, 6, 243–279.
- Johnson, A. (1970), *Physical Processes in Geology: A Method for Interpretation of Natural Phenomena—Intrusions in Igneous Rocks, Fractures and Folds, Flow of Debris and Ice*, 570 pp., W. H. Freeman, New York.
- Lander, J. (1996), Tsunamis affecting Alaska 1737–1996, *Geophys. Record Doc. NOAA NESDIS NGDC 31*, 195 pp., Natl. Oceanic and Atmos. Admin., Silver Spring, Md.
- Liu, K., and C. Mei (1989), Slow spreading of a sheet of Bingham fluid on an inclined plane, *J. Fluid Mech.*, 207, 505–529.
- Locat, J. (2001), Instabilities along ocean margins: A geomorphological and geotechnical perspective, *Mar. Pet. Geol.*, 18, 503–512.
- Locat, J., and H. Lee (2002), Submarine landslides: Advances and challenges, *Can. Geotech. J.*, 39, 193–212.
- Mei, C., and K. Liu (1987), A Bingham-plastic model for a muddy seabed under long waves, *J. Geophys. Res.*, 92, 14,581–14,594.
- Mohrig, D., A. Elverhoi, and G. Parker (1999), Experiments on the relative mobility of muddy subaqueous and subaerial debris flows, and their capacity to remobilize antecedent deposits, *Mar. Geol.*, 154, 117–129.
- Murty, T. (1979), Submarine slide-generated water waves in Kitimat Inlet, British Columbia, *J. Geophys. Res.*, 84, 7777–7779.
- Osher, S., and F. Solomon (1982), Upwind difference schemes for hyperbolic conservation laws, *Math. Comput.*, 38, 339–374.
- Prior, D., B. Bornhold, and D. Johns (1984), Depositional characteristics of a submarine debris flow, *J. Geol.*, 29, 707–727.
- Rabinovich, A., R. Thomson, B. Bornhold, I. Fine, and E. Kulikov (2003), Numerical modelling of tsunamis generated by hypothetical landslides in the Strait of Georgia, British Columbia, *Pure Appl. Geophys.*, 160, 1273–1313.
- Roe, P., and J. Pike (1984), Efficient construction and utilization of approximate Riemann solution, in *Computing Methods in Applied Sciences and Engineering*, vol. 6, edited by R. Glowinski and J. L. Lions, pp. 499–518, Elsevier, New York.
- Skvortsov, A. (2005), Numerical simulation of landslide-generated tsunamis with application to the 1975 failure in Kitimat Arm, British Columbia, Canada, M.S. thesis, Univ. of Victoria, Victoria, B. C., Canada.
- Tappin, D., T. Matsumoto, and Shipboard Scientists (1999), Offshore surveys identify sediment slump as likely cause of devastating Papua New Guinea tsunami, *Eos Trans. AGU*, 80(30), 329, 334, 340.
- Tinti, F. (2002), Needs and perspectives of tsunami research in Europe, *Earth Environ. Sci.*, 21, 9–16.
- Toro, E. (2001), *Shock-Capturing Methods for Free-Surface Flows*, 309 pp., John Wiley, Hoboken, N. J.
- Toro, E., M. Spruce, and W. Speares (1994), Restoration of the contact surface in the HLL-Riemann solver, *Shock Waves*, 4, 25–34.
- van Leer, B. (1977), Towards the ultimate conservative difference scheme III. Upstream-centered finite difference schemes for ideal compressible flow, *J. Comput. Phys.*, 23, 263–275.
- van Leer, B. (1985), On the relation between the upwind-difference schemes of Godunov, Engquist-Osher and Roe, *SIAM J. Sci. Stat. Comput.*, 5, 1–20.
- Wiegel, R., E. Noda, E. Kuba, D. Gee, and G. Tornberg (1970), Water waves generated by landslides in reservoirs, *J. Waterw. Harbors Coastal Eng. Div. Am. Soc. Civ. Eng.*, 96, 307–333.
- Yanenko, N. (1971), *The Method of Fractional Steps*, Springer, New York.

B. Bornhold and A. Skvortsov, School of Earth and Ocean Sciences, University of Victoria, P.O. Box 3055, Victoria, BC, Canada, V8W3P6. (sas6@uvic.ca)